# EIT OBSERVATIONS OF THE EXTREME ULTRAVIOLET SUN

D. MOSES[1], F. CLETTE[2], J.-P. DELABOUDINIÈRE[3], G. E. ARTZNER[3],
M. BOUGNET[3], J. BRUNAUD[3], C. CARABETIAN[3], A. H. GABRIEL[3],
J. F. HOCHEDEZ[3], F. MILLIER[3], X. Y. SONG[3], B. AU[4], K. P. DERE[4],
R. A. HOWARD[4], R. KREPLIN[4], D. J. MICHELS[4], J. M. DEFISE[5], C. JAMAR[5],
P. ROCHUS[5], J. P. CHAUVINEAU[6], J. P. MARIOGE[6], R. C. CATURA[7], J. R. LEMEN[7],
L. SHING[7], R. A. STERN[7], J. B. GURMAN[8], W. M. NEUPERT[8,a], J. NEWMARK[8,b],
B. THOMPSON[8,b], A. MAUCHERAT[9], F. PORTIER-FOZZANI[9], D. BERGHMANS[10],
P. CUGNON[10], E. L. VAN DESSEL[10] and J. R. GABRYL[10]

[1]*Naval Research Laboratory, Washington, DC 20375, U.S.A.*
[2]*Observatoire Royal de Belgique, Brussels, Belgium*
[3]*Institut d'Astrophysique Spatiale, Université Paris XI, 91405 Orsay Cedex, France*
[4]*Naval Research Laboratory, Washington, DC 20375, U.S.A.*
[5]*Centre Spatial de Liège, B4031, Liège, Belgium*
[6]*Institut d'Optique Théorique et Appliquée, 91403 Orsay, France*
[7]*Lockheed Palo Alto Research Laboratory, Palo Alto, CA 94304, U.S.A.*
[8]*NASA/Goddard Space Flight Center, Greenbelt, MD, U.S.A.*
[9]*Laboratoire d'Astronomie Spatiale, Marseille, France*
[10]*Observatoire Royal de Belgique, B-1180 Brussels, Belgium*

**Abstract.** The Extreme Ultraviolet Imaging Telescope (EIT) on board the SOHO spacecraft has been operational since 2 January 1996. EIT observes the Sun over a 45 × 45 arc min field of view in four emission line groups: Fe IX, X, Fe XII, Fe XV, and He II. A post-launch determination of the instrument flatfield, the instrument scattering function, and the instrument aging were necessary for the reduction and analysis of the data. The observed structures and their evolution in each of the four EUV bandpasses are characteristic of the peak emission temperature of the line(s) chosen for that bandpass. Reports on the initial results of a variety of analysis projects demonstrate the range of investigations now underway: EIT provides new observations of the corona in the temperature range of 1 to 2 MK. Temperature studies of the large-scale coronal features extend previous coronagraph work with low-noise temperature maps. Temperatures of radial, extended, plume-like structures in both the polar coronal hole and in a low latitude decaying active region were found to be cooler than the surrounding material. Active region loops were investigated in detail and found to be isothermal for the low loops but hottest at the loop tops for the large loops.

Variability of solar EUV structures, as observed in the EIT time sequences, is pervasive and leads to a re-evaluation of the meaning of the term 'quiet Sun'. Intensity fluctuations in a high cadence sequence of coronal and chromospheric images correspond to a Kolmogorov turbulence spectrum. This can be interpreted in terms of a mixed stochastic or periodic driving of the transition region and the base of the corona. No signature of the photospheric and chromospheric waves is found in spatially averaged power spectra, indicating that these waves do not propagate to the upper atmosphere or are channeled through narrow local magnetic structures covering a small fraction of the solar surface. Polar coronal hole observing campaigns have identified an outflow process with the discovery of transient Fe XII jets. Coronal mass ejection observing campaigns have identified the beginning of a CME in an Fe XII sequence with a near simultaneous filament eruption (seen in absorption), formation of a coronal void and the initiation of a bright outward-moving shell as well as the coronal manifestation of a 'Moreton wave'.

[a] Present address is SEL/NOAA 325 Broadway, Boulder, CO 80303, U.S.A.

[b] Space Applications Corp.

Table I
EIT bandpasses

| Wavelength | Ion | Peak temperature | Observational objective |
|---|---|---|---|
| 304 Å | He II | $8.0 \times 10^4$ K | chromospheric network; coronal holes |
| 171 Å | Fe IX, X | $1.3 \times 10^6$ K | corona/transition region boundary; structures inside coronal holes |
| 195 Å | Fe XII | $1.6 \times 10^6$ K | quiet corona outside coronal holes |
| 284 Å | Fe XV | $2.0 \times 10^6$ K | active regions |

## 1. Introduction

EIT is a new approach for imaging the EUV Sun on an extended spaceflight platform (Delaboudinière *et al.*, 1995). Normal incidence multilayer optics are used to image the Sun on an EUV sensitive 1024 × 1024 format charge coupled device (CCD) camera. With a telescope focal length of 1.652 m and a pixel size of 21 $\mu$m × 21 $\mu$m, the plate scale of the EIT images is 2.6 arc sec per pixel. The optics are divided into quadrants of matched multilayer pairs that are tuned to bandpasses selected for observation of the chromosphere and corona at all phases of the solar cycle. The quadrants are isolated by a rotating mask that permits only one bandpass to view the Sun at a time.

Images from the synoptic program are presented in Figure 1. The full details in these images are inadequately represented in the reduced journal prints, so full resolution digital images are included in the CD-ROM accompanying this volume. The in-flight observations of solar structures match the predictions of Table I (Delaboudinière *et al.*, 1995):

– The Fe IX, X image is generally less structured than the other coronal channels. Diffuse, unresolved emission is present over most of the quiet Sun, including coronal hole regions. Open field structures are seen in this bandpass as well as closed structures. Active region structures, as seen in this channel, are more confined to the core of the active region. Active region loops are narrow structures that in many cases are only filled at the base. These partially filled loops are similar to the 'spiky' Ne VII and Mg IX active region structures observed by *Skylab* (Sheeley, 1980; Webb, 1981). The primary difference is that the Fe IX, X structures do not appear to become narrower with height. A region of supressed emission is frequently observed surrounding an active region. X-ray bright points (XBP) are the most numerous in this channel (by 10%). Detection of faint structures in the Fe IX, X channel is more difficult than in the other coronal channels due to the relative intensity of the quiet corona (including coronal holes).

– The Fe XII image is more dominated by the closed field regions of the quiet-Sun. All but the hottest active region loops are visible in this wavelength. As in the Fe IX, X channel, some active region loops appear to only be partially filled. The appearance of some active regions in Fe XII is that the loops diverge more
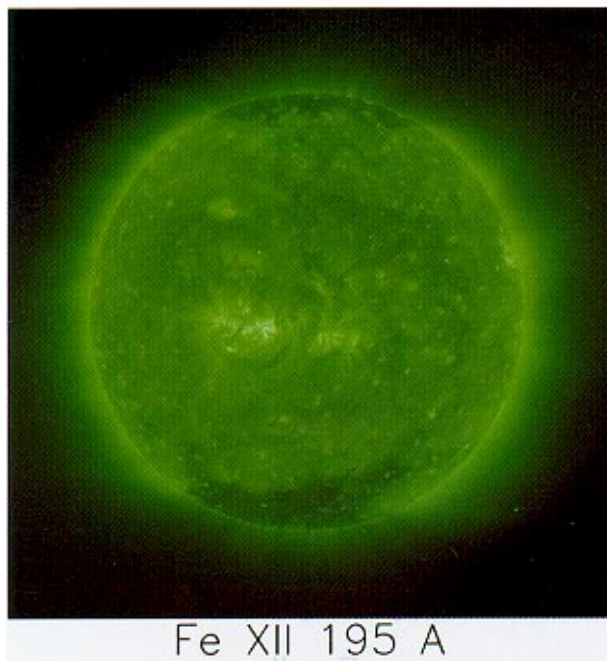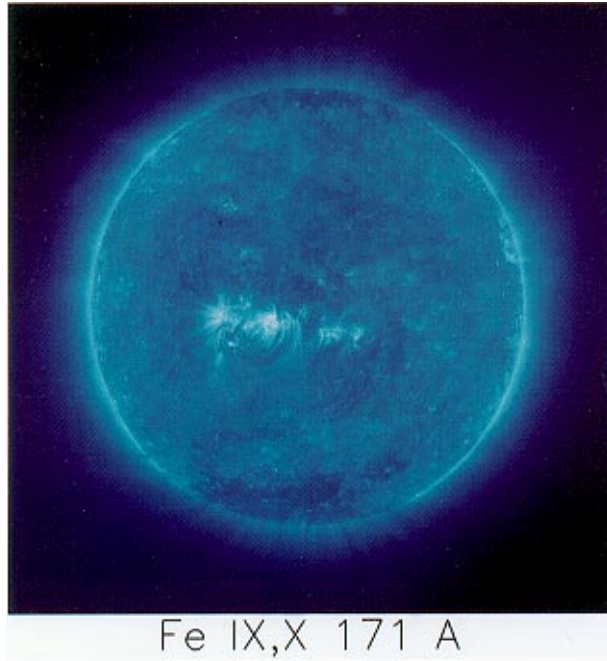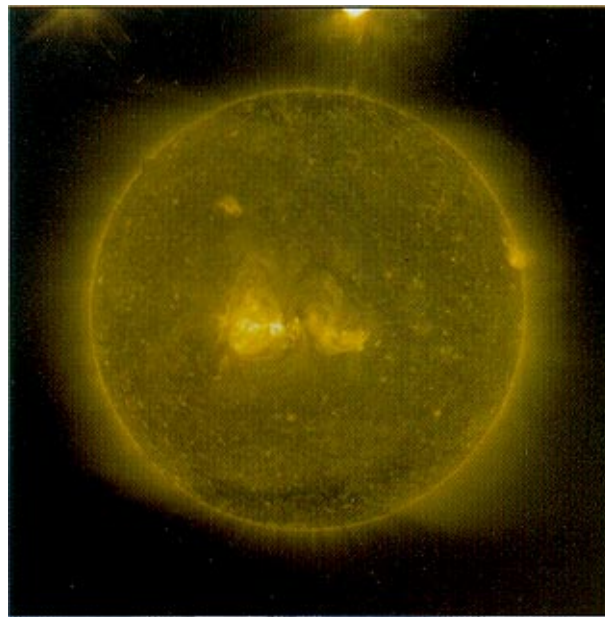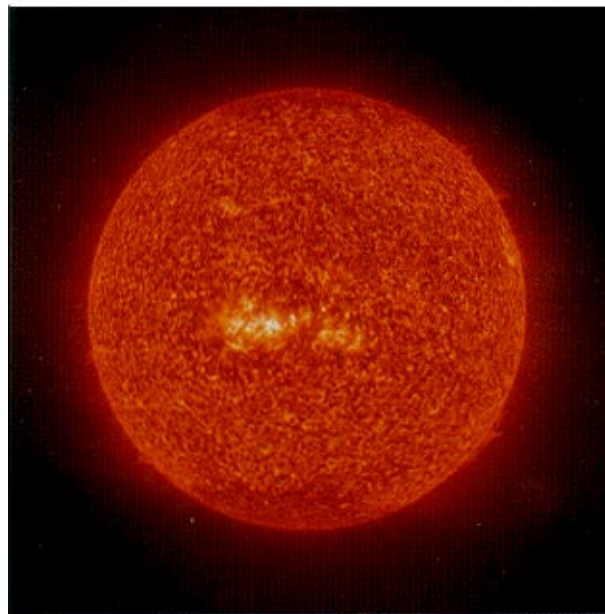
Figure 1a.

Fe XV 284 A



He II 304 A

*Figure 1b.*

*Figure 1.* EIT synoptic images for 12 May 1996. Solar north is oriented up in this figure.

than higher-temperature active region loops (Fe XV and *Yohkoh* SXT). However, application of the technique of Klimchuk *et al.* (1992) on an isolated loop resulted in the same constant cross section for that loop as found at higher temperatures (Klimchuk, Moses, and Portier, 1997). Coronal holes are most easily visible in this channel because of the contrast between the emission intensity of the open field region and the closed field quiet Sun. Similarly, XBPs are most easily identified in this channel because of the contrast between the emission associated with the XBP magnetic bipole and the emission associated with the relatively weaker quiet-Sun magnetic regions or the coronal hole open field regions. Because of the high contrast and the high sensitivity to quiet Sun structures of the Fe XII channel, it is frequently used for movies of coronal evolution.

– The Fe XV image is dominated by the hot loops (e.g., active region loops). Of all the EIT observations, these most closely compare with the *Yohkoh* SXT images. Outside the active regions, this emission is obvious in the X-ray bright points, regions of erupting filaments and large-scale height loop structures. The large-scale height structures are best visible above the limb. In quiet Sun regions, there is also low level structure in Fe XV that maps out some of the internetwork field structure. The quiet-Sun Fe XV structure is not leakage of the He II into this channel as it does not form a complete network structure and cannot be removed by a normalized subtraction of a He II image. Instead, it is the high temperature component of the more general, diffuse emission seen in the other coronal channels. Also apparent in this channel is a visible light leak at the north edge of the field of view which is discussed in Section 3.

– The He II image is dominated by the transition region network structure. Bright network elements are visible throughout the region of closed loop structures. The coronal holes are marked by a reduction in the He II network elements. Active regions are generally bright in the He II image with a blending of Si XI emission. A region of supressed emission is frequently observed immediately around the active region enhancements. Macrospicules are apparent in the open field regions and along some large-scale closed regions. They are apparently aligned with the direction of the magnetic field. Prominences are always present. Filaments are slightly more difficult to identify because the contrast of the absorption features is frequently comparable to the contrast of the network structure.

Intercomparison of the images from the different coronal channels shows that, with increasing temperature, the plasma is more structured. As will be discussed in section 2.2, with increasing temperature for all channels, the emission exhibits greater variability with solar activity (time).

Detailed comparison of quiet Sun regions of coronal images and the He II images (e.g., Figure 11 in Section 3.2) shows that there is a transition region enhancement for every enhancement of coronal emission, but not the converse. This is in agreement with previous comparisons of X-ray bright points and He I 10830 Å emission (e.g., Moses *et al.*, 1994). With the availability of near-continuous photospheric magnetic field data from SOHO, the assumption that the relationship

between the coronal counterparts of transition region features and the connectivity of the magnetic field can now be addressed.

A comparison of the appearance of prominences and filaments in the four EIT channels can be made from Figure 2. On the equator, the prominence is aligned primarily perpendicular to the line of sight. This structure can be seen in absorption in the coronal channel due to a combination of H I, He I and He II continuum absorption (Cheng, Smith, and Tandberg-Hanssen, 1980; Foukal, 1978; Schmahl and Orrall, 1979). The prominence in the south east can be seen to extend onto the disk as a polar crown filament in the He II as well as in the coronal channels. There is a coronal void around this prominence which reflects the temperature structure of the corona and is not due to absorption. The amount of absorption in the coronal lines depends upon the observed wavelength, the overall geometry of the observation, the relative elemental abundance, the density and the ionization balance of the cool material and thus can be used as a diagnostic of the plasma parameters of prominences.

## 2. Instrumentation

To move beyond a descriptive analysis of the data, several instrument issues must be addressed. These issues were either impossible to resolve pre-launch or their importance was not appreciated before the initial analysis began. This work has taken a large part of the EIT consortium effort during the first year of operations.

### 2.1. IMAGING

The images obtained in-flight by EIT are consistent with the assertion by Delaboudinière *et al.* (1995) that the instrument resolution is limited by the plate scale of the CCD. Analysis of the off-disk images raises interesting questions about the extended distribution of He II in the solar atmosphere (Delaboudinière, 1998). In order to quantify these observations, the wings of the point response function (PRF) must be known in the EUV to better than the dynamic range of the CCD (1:5000). The PRF has been evaluated with wavefronts obtained with Zygo interferometer measurements of the telescope in each quadrant. The wavefronts obtained at 6330 È were converted into optical path differences to obtain the complex pupil function. The Fourier transform of the complex pupil function gave the point spread functions of the optics in the four EUV wavelengths. The system PRF was obtained after convolution with the pixel size. Figure 3 is a plot of 2 perpendicular cuts in the PRF determined by the wavefront analysis for the 284 È quadrant. (N.B. The quadrant structure of the telescope entrance pupil produces an asymmetric PRF.) To verify the Zygo measurements with measurements in the EUV, modifications were made in the IAS calibration facility in an attempt to produce a point source in the EUV with large angle scattering less than the level to be measured. The
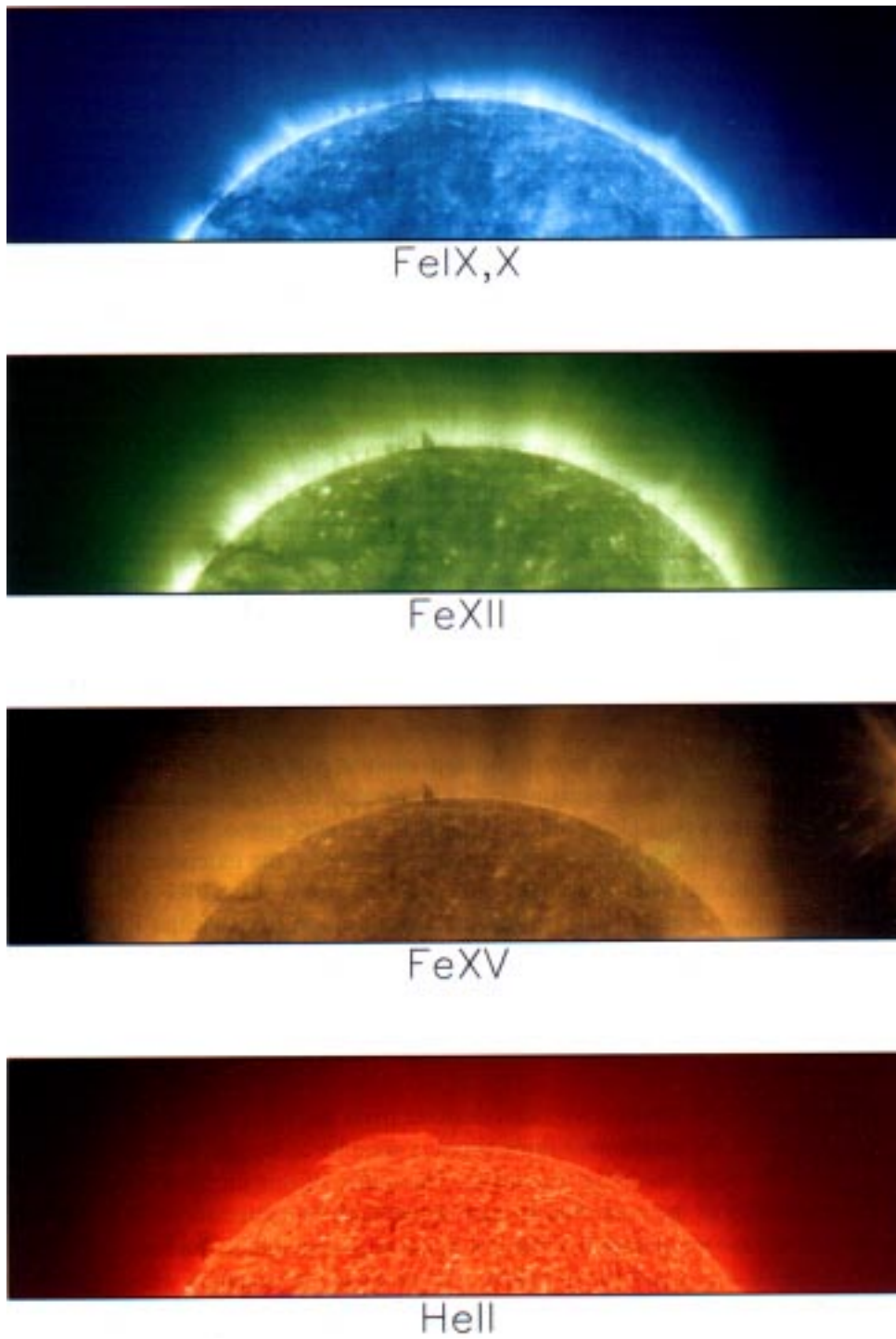
FeIX,X

FeXII

FeXV

HeII

*Figure 2*. H I, He I, and He II absorption features in the EUV coronal images of the east limb on 28 February 1997.
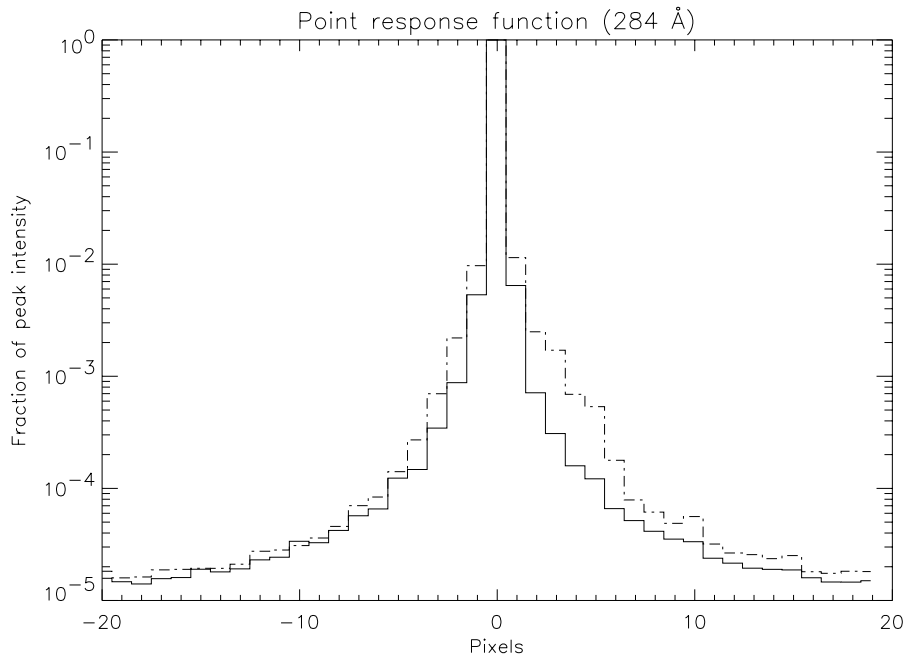
*Figure 3*. EIT extended point response function for the 284 È quadrant from a wavefront analysis. The two lines represent perpendicular cuts through the peak of the response.

spare EIT optics were tested in this configuration as part of the EIT Calroc sounding rocket program. These measurements confirmed the Zygo wavefront analysis result that the far wings (1 arc min) of the PRF are suppressed by nearly 5 orders of magnitude relative to the core. However, vibration in the extended IAS facility prevented reliable measurement in the EUV near the core of the PRF. Observations of active regions in Fe XV just behind the solar limb verify that the EUV scatter measurements at IAS overestimate the spread of the PRF near the core.

## 2.2. EUV RESPONSE

Optimized exposure times have been derived from the inflight images (Table II). The variation of the instrument throughput is monitored by the total flux in a full field image for each bandpass (Figure 4). The utility of this monitor is determined by the variability of the solar flux in each waveband. The intrinsic solar variability increases with the temperature of the dominant emission line in the bandpass. Thus the monitor is very good for the He II and the Fe IX, X channels where the solar variability is low, while it degrades for the Fe XII channel and is poor for the Fe XV channel where changes in the instrumental response are masked by solar changes. Since the extremes of the wavelength regime are 171 È (Fe IX, X) and 304 È (He II),
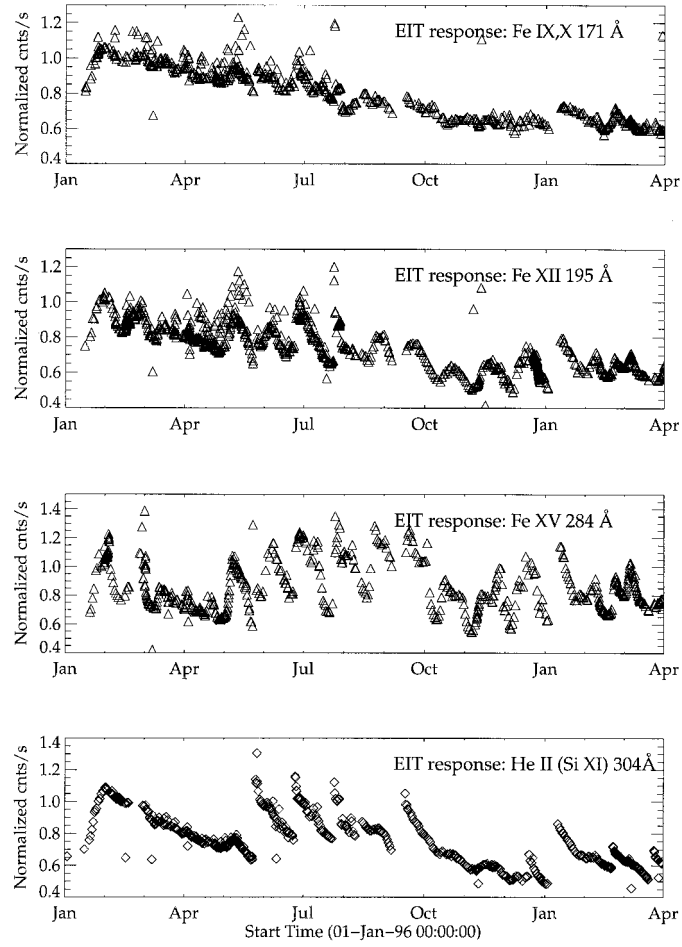
*Figure 4.* EIT response: total flux in each channel.

Table II
Nominal exposure times

| Channel | Quiet Sun | Low activity | High activity |
|---------|-----------|--------------|---------------|
| He II | 32 s | 25 s | 18 s |
| Fe XI, X | 7 s | 5.5 s | 2 s |
| Fe XII | 12 s | 9 s | 4 s |
| Fe XV | 102 s | 62 s | 47 s |

this technique allows the full wavelength dependence of the degradation to be monitored.

Since the 304 È radiation has the lowest penetration depth (range) of the wavelengths observed, the He II channel is the most sensitive to degradation asso-

Table III
EIT CCD temperature cycle history

| Action | Date and Time | Duration |
|---|---|---|
| Heater on | 1996 23 May 19:21 | 45 hr |
| Heater on | 1996 23 June 19:10 | 24 hr |
| Heater on | 1996 23 July 15:48 | 2.5 hr |
| Heater on | 1996　5 Aug 18:50 | 15 hr |
| Heater on | 1996　9 Aug 15:05 | 71.5 hr |
| Heater on | 1996　6 Sep 19:49 | 236 hr |
| Heater on | 1996 19 Dec 13:14 | 2.5 hr |
| Heater on | 1997　3 January 21:50 | 156 hr |
| Heater on | 1997 20 February 21:57 | 13 hr |

ciated with evolution of surfaces and best illustrates the operative processes. The initial increase in response over the first month of observations is attributed to an overall cleanup of the optical surfaces and detector from the contamination associated with the launch and early spacecraft operations. Subsequently the response declined exponentially with an $e$-folding time of 210 days. In order to reverse the decline, the CCD was heated to 18C on 23 May 1996. Initial recovery was to the highest throughput observed in flight. Subsequent response declines have a shorter $e$-folding time (85 days) than the initial February to May interval. Successive heat cycles were conducted according to the requirements of the observing schedules and in exploration of the causes of the decline (Table III). An instrument failure occurred on 29 July that left the shutter open in the 304 È channel for 7 hours. The total instrument response immediately declined 10 to 20% following this exposure. The response degradation was not uniform. Instead the degradation was patterned in proportion to the EUV exposure.

The degradation process consists of several components which are difficult to separate in detail. The two basic processes contributing to the degradation are (1) the absorption of EUV before it interacts with the CCD by a surface contaminant and (2) the reduction of charge collection efficiency (CCE) in the CCD due to EUV induced device damage.

The condensation of contaminant on the CCD is expected since the detector is one of the coldest surfaces in the instrument. In anticipation of in-flight contamination, (1) a cleanliness program was maintained in the construction of the instrument and (2) heaters for the CCD were included in the design. Accumulation of contamination at a constant rate will result in an exponential decline in response. If no polymerization of an organic component is involved, then the condensate will evaporate rapidly during temperature cycling. The straylight baffling around the CCD unfortunately reduces the vacuum conductance out of the vicinity of the CCD so that further outgassing during a temperature cycle is not feasible.

Reduction of the CCE is probably caused by the charging of the native backside oxide and the generation of interface trap sites. Since each interacting EUV photon generates more than one electron, the CCE can be determined by the comparison of the observed signal to the photon shot noise (Janesick, Klassen, and Elliott, 1987). The limitations of this approach are significant, but the degradation of the device for the 29 July event has been demonstrated to be totally CCE degradation. The proportion of the cumulative degradation from ordinary operations which can be attributed to CCE degradation is discussed in Defise *et al.* (1997). Although self annealing is observed, the rate of self annealing is dependent on the device temperature and possibly the level of prior damage. The self-annealing process during temperature cycling is at best 100 times slower than the condensate reversal.

## 2.3. FLAT-FIELD CORRECTIONS

Spatial variations of the instrument response across the field of view must be corrected before performing almost any quantitative analysis of EIT images. These non-uniformities are produced by several independent contributions. Some of these flat-field components were known before SOHO launch, like the optical vignetting, the CCD flat-field and the grid pattern produced by the focal aluminum filter. However, the grid pattern could only be accurately measured after launch, using in-flight solar images. Moreover, during the course of the mission, two unpredictable artifacts appeared: a light leak affecting mainly the Fe XV images and a radiation induced non-uniform degradation of the CCD response. The characteristics of these last components can only be indirectly deduced from the affected solar images themselves, which limits the accuracy of any reconstruction due to the incomplete or distorted information available from flight data. Consequently, the ambitious 1% target for the accuracy of each flat-field component will not be met for some of them.

### 2.3.1. *The CCD Flat-Field*
A CCD flat-field calibration at EIT's working wavelengths was obtained on the ground with a monochromatic beam of synchrotron radiation using the method developed by Kuhn, Lin, and Loranz (1991). This analysis has been extended from the initial work reported in Delaboudinière *et al.* (1995). Figure 5 shows large-scale trends of the CCD flat field. Of particular interest is the steady gain enhancement towards the sensor edges, that reaches an amplitude of 10 to 15%. This last feature went unnoticed in a first partial analysis (Delaboudinière *et al.*, 1995). The accurate determination of these large-scale variations required special care, as the Kuhn, Lin and Loranz algorithm can produce false linear trends when intensities in the input images are improperly scaled. The accuracy of calculated large-scale variations was verified, but any residual edge-to-edge slope cannot be determined to better than about 10%. At smaller spatial scales, the accuracy of the results is close to 1%.
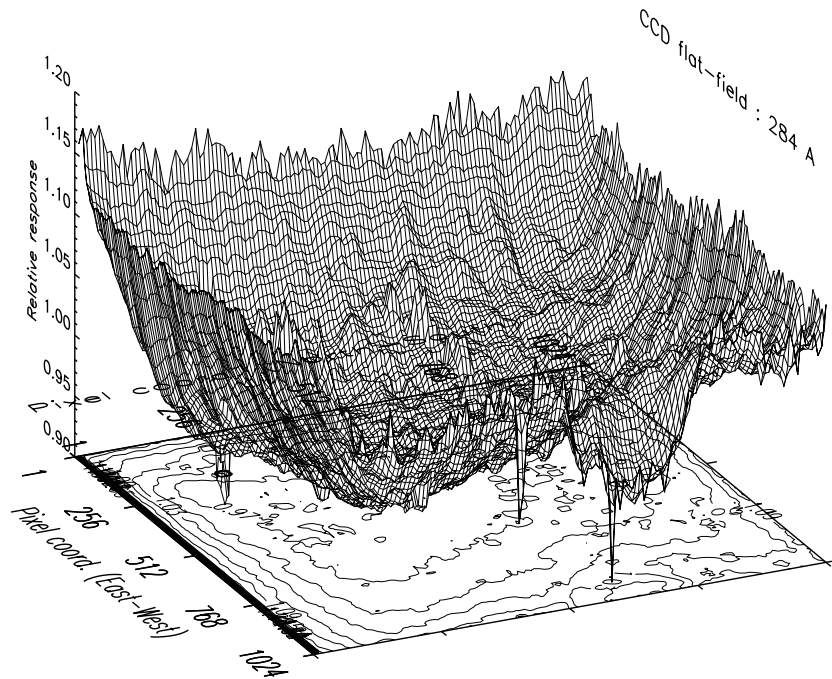
*Figure 5.* Three-dimensional plot of the CCD flat-field, showing the amplitude of the large-scale gain variations. The original map was smoothed over a 24 × 24-pixel domain to suppress local fluctuations.

Although the flat-field shows little change with wavelength, a systematic 10% increase in the amplitude of the defects can be measured from 171 È to 304 È. A comparison of the ground-based flat-fields with those deduced from the in-flight solar images shows a very good agreement over most of the sensor. However, significant discrepancies are observed inside some of the larger blemishes. Contaminants apparently interact preferentially with the surface defects. This could be interpreted in one of two ways: (1) the defects act as condensation nuclei or seeds for microcrystal formation or (2) the electronic properties of the defects are activated by chemical interaction with the condensate. Further analysis is needed to reconcile both measurements over the whole CCD within the 1% accuracy of the calculation. However, if we exclude the radiation induced aging described below, no change of the intrinsic CCD flat-field was detected in in-flight images during the first year in space.

### 2.3.2. *The Al-Filter Grid Pattern*

One of the redundant aluminum filters used to block long-wavelength radiation (mainly visible light) is located 14.5 mm in front of the CCD detector. Such Al filters are mechanically supported by a nickel grid (Delaboudinière *et al.*, 1995) which casts a shadow on the CCD. The finite extent of the asymmetrical entrance pupil of the telescope produces a smoothed out-of-focus pattern. The resulting

periodic intensity modulation, with an amplitude of about 15%, proved to be the main flat-field artifact. Another set of filters is located on a filter wheel, 35 mm in front of the CCD. When an additional Al filter is selected on the filter wheel, it produces an additional grid pattern, with different characteristics, as it is located at a larger distance from the focal plane.

In order to extract the grid pattern from the solar images themselves, we relied on the fact that the pattern is purely periodic, while the spatial distribution of the intensity on the EUV Sun is essentially random (Note that the Sun acts as a noise source in this problem). The extraction process consists of the following steps:

– Full-field full-resolution daily synoptic images are averaged over a period of several weeks (rotational averaging of activity features). The sensor noise is also reduced by this averaging.

– The average image is then submitted to a non-linear filtering: a running 2-dimensional median filter is applied to $5 \times 5$ pixel sets, with a 21-pixel spacing between sampled pixels in both dimensions. As this 21-pixel interval is a close approximation of the grid period, the filter selectively amplifies the grid signal relative to all other spatial fluctuations in the image, i.e., it acts as a morphological filter.

– The Fourier transform of the resulting image reveals about 30 peaks, corresponding to the harmonics of the grid pattern. Two numerical filters are then applied in the frequency domain : suppression of the low-frequency $f^{-1}$ noise background (subtraction of a smoothed average radial profile) and rejection of high-frequency noise in regions where no harmonics are present (square domains with cosine edge tapers).

– An inverse transform is finally applied to the filtered spectrum to reconstruct a cleaned image of the grid modulation.

The resulting pattern has the regularity and uniformity expected from the grid specifications (mesh period: 440 $\mu$m, mesh width: 40 $\mu$m). The grid is detected up to the very corners of the field of view, despite the very low signal levels in that part of the solar images. The grid corrections, which are now integrated in the EIT image display software, are accurate to about 1% over most of the field of view.

Diffraction calculations indicate a slight wavelength dependency, with a 5% increase of the modulation amplitude between 171 and 304 È. However, the 90° rotation of the pattern for each EIT bandpass, following the changing orientation of the entrance pupil, produces most of the observed differences. Comparative measurements do not reveal significant temporal changes in the grid pattern since the beginning of the mission.

### 2.3.3. *Filter Pinholes and Visible-Light Leak*

Two light leaks were discovered early in the mission. They affect mainly the Fe XV and also to a lesser extent (50 : 1) the Fe IX, X images in the 'Clear' filter wheel position. Both leaks are located near the northern edge of the images and consist a bright featureless core surrounded by fainter halos containing sharp rays and
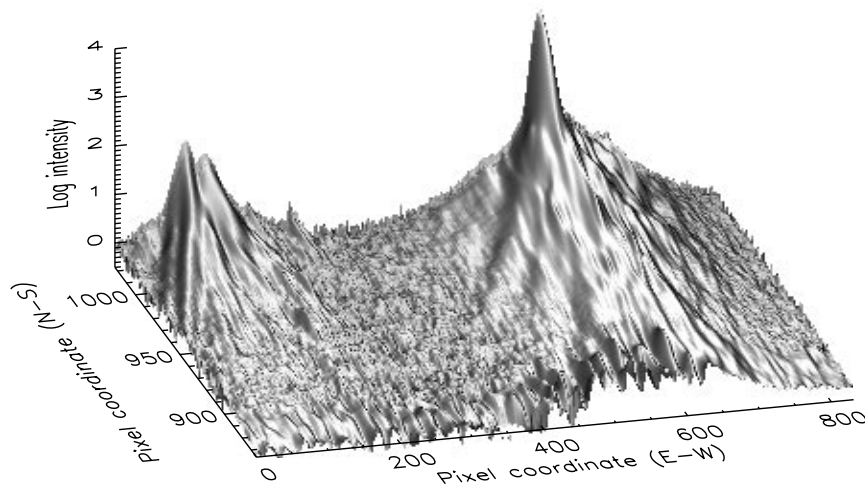
*Figure 6.* Two-dimensional distribution of the stray-light intensity produced by the light leaks in the 832×160 upper left area of the field of view, at 284 È. To compensate the large intensity range between the core and faint extensions, several stepped exposures were combined and a logarithmic intensity scale is used. The intensities are scaled here according to the raw sensor output signal for a 10 s exposure.

extending up to 150 pixels from the core (Figure 6). No leak is detected in the Fe XII and He II images.

These leaks can be attributed to minute pinholes at the edge of the focal Al filter, and the light passing through these holes has been unambiguously identified as visible light reaching the CCD by study of the statistical fluctuations (photon shot noise dominated) of the signal. The visible light pattern is superimposed on the EUV solar image. The presence of visible light reaching the focal filter further implies the existence of visible light leaks in the entrance Al filters. Considering the large visible/EUV flux ratio and the limited intensity reaching the focal plane, both filter defects must affect only a small fraction of the filter area. These degradations probably occurred during SOHO's launch. The relative intensity of those leaks (50 : 1) at each of the two wavelengths, i.e., at each sector position, allow us to deduce that the tear in the front filter is located in the Fe XV sector near the edge adjacent to the neighboring Fe IX, X sector.

Being very bright and located in the dim and fairly uniform polar corona, this additive component can be extracted with a high accuracy from the Fe XV images. No significant changes in the pattern were observed in the course of the mission.

### 2.3.4. *Spatial Distribution of Radiation Induced Aging*
A degradation of the CCD response is induced by the radiation dose received by the detector, as explained in Section 2.2. As the average EUV intensity in the coronal and transition region images is highly non-uniform, the calculated flat-field is distorted by strong residuals of local solar activity features, especially outside the

disk area. Figure 7 illustrates the distribution of the radiation damage as it appeared in mid-December 1996. While the response remains largely unaffected far from the solar limb, the degradation is strong (50% in this case) over the solar disk, in the form of a negative imprint of an average solar disk. A slight limb darkening can be recognized as well as a single grid pattern, which coincides with the 304 È (He II) grid pattern. All these properties indicate that most of the degradation was primarily produced by the long-wavelength radiation at 304 È, with significantly less contribution from the exposures made in all three coronal lines. (The Fe XII and Fe IX, X exposures are at shorter wavelengths, and the total dose in the Fe XV is low in comparison to the other channels). Moreover, the localized damage due to the active region located near the S−E limb at the time of the 29 July 1996 shutter failure can also be recognized. The largest damages are found within this region, where the response falls to about 20% of its average value on the rest of the disk. Finally, as the radiation damage is averaged over long periods, the changing apparent solar radius produces a smoothed limb profile. As the integrated damage always lags behind the actual solar radius, this can produce a spurious limb brightening or darkening in uncorrected images.

The successive CCD bakeouts carried out since late May 1996 have shown that the damage can be partly cured by this method (cf., Section 2.2). However, the degree of recovery is variable over the field of view and also from one bakeout to the next. Indeed, from the limited information derived from the few bakeouts executed so far, we can already deduce that the CCD response is affected by different radiation-induced mechanisms having different properties. The magnitude of each effect also depends on the time span separating successive bakeouts and their response to bakeout is strongly variable. Some components disappear completely in a few hours (e.g., small off-limb effects), while others remain relatively unaffected (e.g., active region blemish).

Two techniques are now available to monitor changes in the spatial evolution of the radiation damage:

– Reconstruction of the EUV response from sets of solar images. An adaptive median filtering is applied, which again makes use of the rotational averaging effect. This the only way to extract the true EUV response. However, the accuracy of the reconstruction is low, due to the permanent changes in the solar images.

– Calibration lamp images. In this case, a diffuse illumination is provided by a lamp located next to the CCD. This illumination proved to be very stable with time, but it falls in the visible and near-infrared wavelength ranges. The CCD response can be very different at these long wavelengths, and comparisons with EUV results have even shown that some components affecting the EUV response escape detection in the calibration lamp images.

Considering their respective drawbacks, both approaches must be combined to improve the accuracy of the reconstruction. However, in view of the continuous evolution of this aging effect, it might be difficult to reach an accuracy better than 5%. For instance, preliminary EUV − visible comparisons also hint at the super-
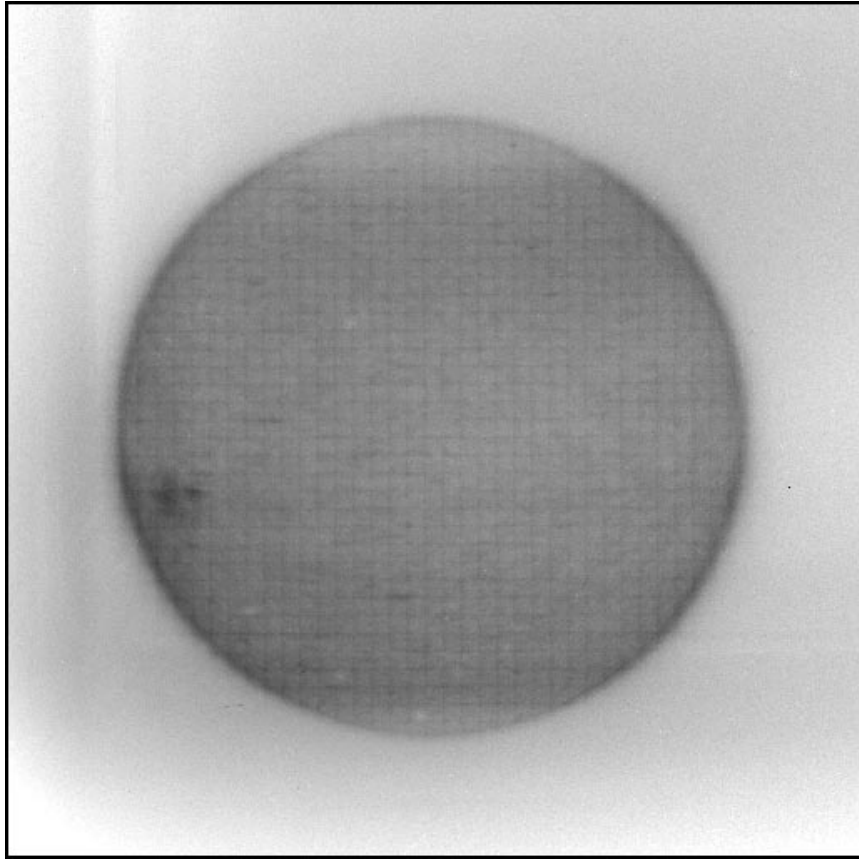
*Figure 7.* Distribution of the radiation induced aging of EIT's CCD sensor on 19 December 1996. This image was obtained by taking the ratio between calibration lamp images made in December 1996 and June 1996, when the response was still almost uniform.

position of different factors affecting differently the detector sensitivity in either wavelength range. Further analysis is in progress and should help in the identification of the underlying physical mechanisms (opacification of surface contaminants or degradation of the CCD charge collection efficiency: see Section 2.2). The ultimate goal of this effort would be to build a consistent model of the radiation damage. This fundamental undertaking will rely heavily on a permanent monitoring of the accumulated radiation dose and of the corresponding changes in the uniformity of the CCD response, which will be pursued until the end of the mission.

## 3. Observations

The versatility of the EIT instrument and the organization of the SOHO Experiment Operations Facility (EOF) allow a diverse range of scientific investigations. The

EIT synoptic program consists of one full frame full resolution image in each waveband each day. In addition, EIT supports SOHO Joint Operations Programs (JOPs) involving the coordinated observation of targets with the other SOHO instruments and outside observational facilities. EIT is deeply involved in the SOHO JOP program because of the context provided by a full disk EUV image. The results of the JOP participation are extremely diverse and are outside the scope of this paper. Beyond the synoptic program and JOPs, special EIT observing programs are conducted.

In this section we present reports of some of the new results from the EIT science investigations. The temperature structure of the corona is the subject of the first two sections. From the synopic program, the large-scale thermal structure of the corona in the temperature regime of 1 to 2 Mk is described in Section 3.1. In order to investigate in detail the thermal structure with height of an active region, a special observing sequence was executed for an active region on the limb (Section 3.2).

The variability of the upper chromosphere and corona is well observed with EIT image sequences and is the subject of the last three sections. In Section 3.3, movies in the He II and Fe XII channels show the dynamics of the EUV Sun. An analysis of the variability in these channels during a special high-cadence observing program is presented in this section. Sequences dedicated to identifying outflows and eruptions are the subject of Sections 3.4 and 3.5. Programs searching for evolution of coronal plumes have recorded dynamic events in the polar coronal holes which are labeled 'EUV jets'. Programs searching for the initiation of coronal mass ejections have identified these events in the EIT images.

## 3.1. CORONAL TEMPERATURE DIAGNOSTICS

Although many observations and much analysis exists on coronal structures at temperatures up to about 1 MK and above 2 MK, principally from EUV and soft X-ray observations by *Skylab*, SMM and *Yohkoh*, less attention has been directed toward the EUV structure of the corona between 1 and 1.5 MK where soft X-ray imagers have relatively little sensitivity. Initial observations from EIT confirm that this is an uniquely interesting temperature regime, particularly during the interval of solar minimum activity.

The three EIT coronal imaging channels were designed for optimum coverage of the temperature range of 1.0 to 2.5 MK. Each coronal bandpass was chosen to be dominated by a different ionization state of Fe under specific conditions (e.g., non-flaring structures in the Fe XII channel), so that abundance variations would not be a factor in the relative fluxes observed in each channel. The assignment of a plasma temperature value to a given set of fluxes observed in the three channels in a given pixel is, mathematically, a poorly constrained inversion problem requiring a set of assumptions, including the cospatiality of material being observed in optically thin lines. However, with sufficient attention to the limitations of this approach, the

thermal distribution and evolution of the corona in this temperature regime can be explored.

### 3.1.1. *Morphology of Line Ratio Maps*

Before quantitative analysis is presented, it is instructive to investigate the morphology of maps of the ratio of the Fe XII and Fe IX, X channels as a guide to the overall temperature distribution of 1 to 2 MK plasma in the corona. These two spectral bands have peak sensitivity at 1.2 MK and 1.5 MK, respectively, sufficiently close that cospatiality of at least some features can be expected. Even in the circumstance that the emission regions are not cospatial in the two channels, the relative intensity of the channels indicates the relative thermal distribution in the corona. The thermal distribution of coronal plasma in the 1 to 2 MK regime is presented for 12 May 1996 in Figure 8. Note the residual grid pattern in Figure 8. The aluminum filter support grid shadow discussed in Section 2.3 would dominate the ratio image without correction. This demonstrates the importance of the instrument work described in Section 2 even for qualitative analysis.

This ratio map generally outlines magnetically closed field regions. The diffuse, unresolved coronal regions in the Fe XII and Fe IX, X channels are cooler than the structures associated with stronger field regions and are thus also dark in the ratio image. For this reason, the ratio maps are sometimes used for enhanced contrast coronal displays for easy comparison with other data. X-ray bright points are associated with compact bipolar regions and are identified in the ratio image as bright compact structures. Active regions are indicated as the hottest structures observed on the disk by their intensity in the ratio image.

The coronal hole regions are clearly defined as cool, open field regions by the dark regions in the ratio image both on and off the disk. Polar plumes are identified in the ratio images as the darkest and thus the coolest structures in coronal holes. Plume-like structures have been observed outside the polar holes (see below for an example in a decaying active region) and they are some of the coolest extended coronal structures observed by EIT.

Closed off-limb regions in the ratio map are predominantly indicative of large-scale structures because the increased line of sight reduces the contribution of any given compact structure. In general, the extended, closed-field structures seen off-limb in the ratio images are hotter than the corresponding on-disk structures because the line of sight is primarily integrating through the region of higher temperature plasma which has a greater scale height. Extended structures outlined by the ratio maps include both high-latitude and low-latitude structures.

### 3.1.2. *Coronagraph Comparisons*

The hot high-latitude structures observed in the EIT temperature maps correspond to the persistent closed loop structures seen in the LASCO C1 green line (Fe XIV) coronagraph images as reported by Schwenn *et al.* (1997). These structures are of particular interest because of their role in determining the characteristics of the
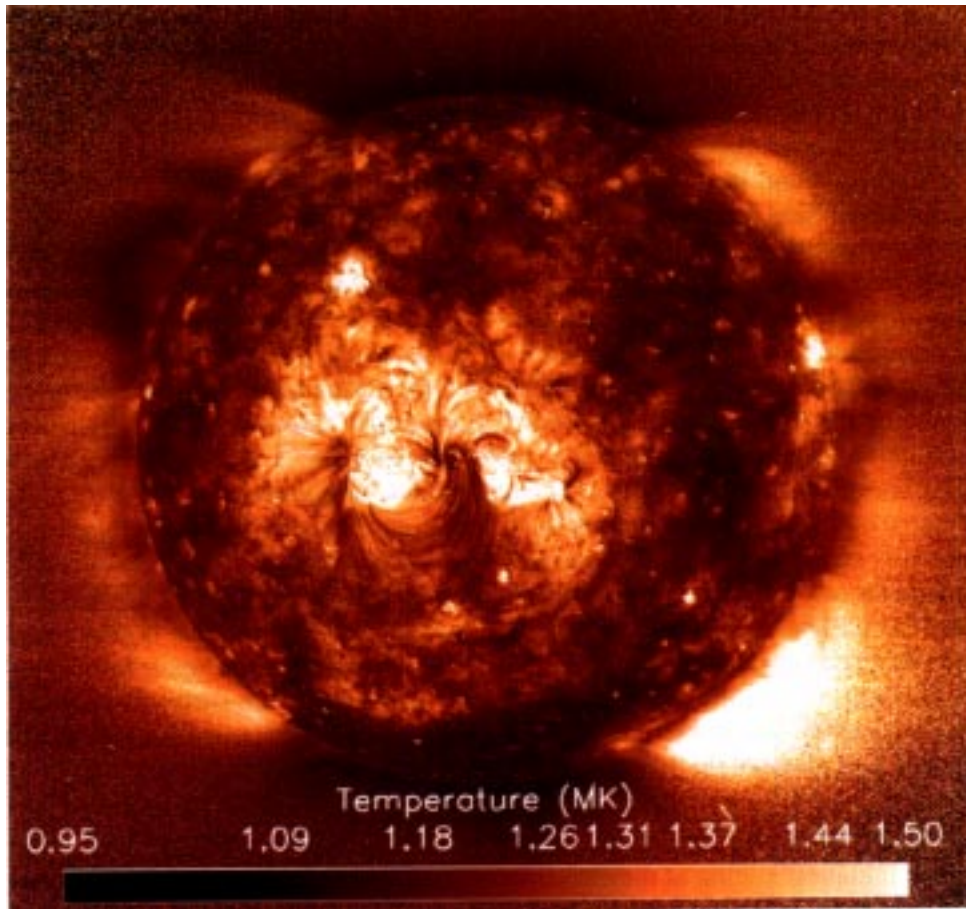
*Figure 8.* Temperature map derived from ratio of Fe XII and Fe IX, X from 12 May 1996

heliospheric current sheet. This correspondence directly links these high latitude structures with the large-scale high-temperature zones observed by Guhathakurta and Fisher (1994) using ground based green line (Fe XIV) and red line (Fe X) ratios. With the improved signal to noise ratio of the EIT temperature maps and the capability to follow a structure as it rotates on or off the solar disk, the EIT observations provide a valuable enhancement to the work with coronagraphs on this topic.

The *high-latitude* off-limb large-scale structures observed by EIT show a coupling of emission intensity and temperature. Comparable structures observed in the study by Guhathakurta and Fisher show the same coupling throughout most of the last solar cycle. With the low-noise EIT temperature maps, a temperature enhancement of these high-latitude structures at the boundary with the polar hole can frequently be observed. This can be seen in the both southern polar hole boundar-

ies and the westward northern polar hole boundary of Figure 8. These temperature enhancements are also identified as regions of enhanced emission. As such, this temperature enhancement is better interpreted as a high-latitude concentration of closed-field flux elements than as some example of increased heating in the region of transition from closed to open field magnetic geometry.

Also, as found in the Guhathakurta and Fisher study, the *low-latitude* large-scale closed field structures observed by EIT do not show as direct coupling of emission intensity and temperature. This is particularly true for the case of structures associated with an active region surrounded by a weak magnetic field region. Due to the higher density of the active region loops, this is observed on the disk as well as on the limb. With the on-disk view of these structures, their magnetic origins can be determined. The region of enhanced temperature associated with the active region on the disk in Figure 8 is clearly much larger than the region of enhanced emission associated with the active region in the Fe IX, X and Fe XII images. A close examination of the Fe IX, X images shows, in comparison to the intensity of the overall quiet-Sun emission in this line, an extended region of suppressed emission surrounding the active region. Interestingly, there is also a kind of 'moat' around the active region in He II suggestive of the H$\alpha$ circumfaculaire described by Bumba and Howard (1965). Apparently, flux elements in an active region which have diffused far enough from the neutral line of the active region bipole form large-scale connections with opposite polarity flux elements in the surrounding mixed polarity region. The consequence is a region of large-scale structures beyond the temperature range of the Fe IX, X images.

### 3.1.3. *Quantitative Analysis*

For an initial estimation of the emission measure and temperature of the structures observed by EIT, the preflight calibration described in Delaboudinière *et al.* (1995) has been combined with the CHIANTI solar spectrum (Newmark *et al.*, 1996). The CHIANTI (Dere *et al.*, 1997) database is maintained on the world wide web for easy access by the astrophysical spectroscopy community:

– http://wwwsolar.nrl.navy.mil/chianti.html.

With the limitations in applicability of the pre-flight EIT calibration described in Section 2 above, the results of this calculation must be considered preliminary until the conclusion of inflight intercalibrations involving the EIT Calroc and SEM CALSO–3 sounding rocket programs and the SOHO CDS, SUMER, CELIAS/SEM and UVCS. At this stage of analysis, it is preferable to just consider ratios of bandpasses. The temperature sensitivity for a unit emission measure of ratios of the three coronal channels is presented in Figure 9. Although all of the curves become double valued at higher temperatures, the response of the instrument to these higher temperatures is so low (Delaboudinière *et al.*, 1995) that these regimes become important only for hot regions of very high emission (e.g., flares).

In the images of 12 May 1996 from Figure 8 above, one can identify several interesting regions in the Fe IX, X and Fe XII images that are straightforward to

Table IV
Plasma parameter calculations

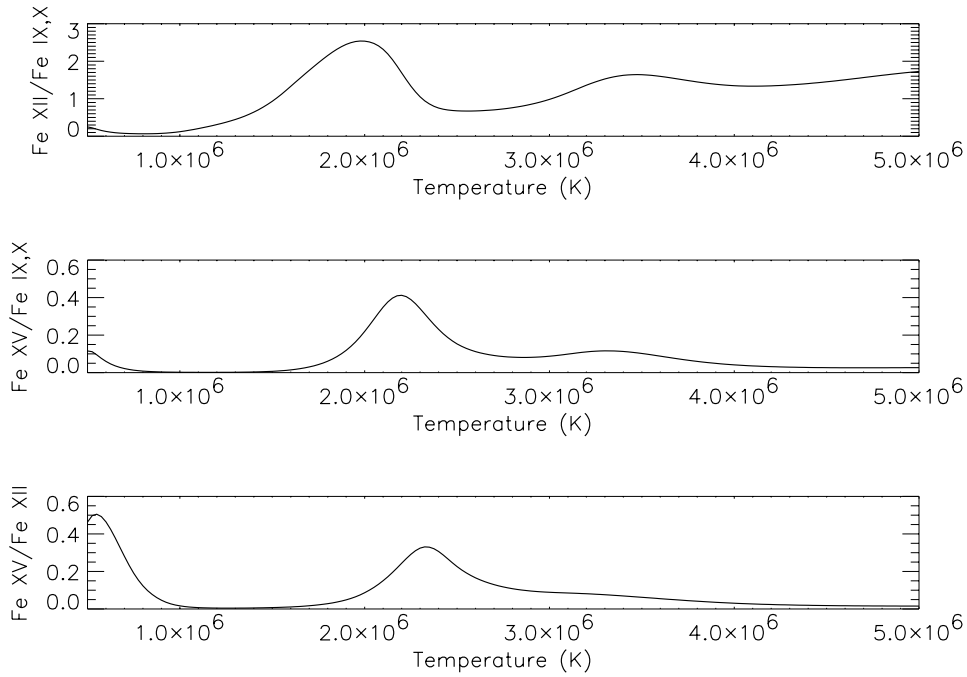| Feature | Counts $s^{-1}$ (195 Å) | Fe XII/Fe IX, X | Temp $\times 10^6$ K | EM ($cm^{-5}$) |
|---------|---------|---------|---------|---------|
| Plume (base) | 50 | 0.55 | 1.35 | $7 \times 10^{27}$ |
| Coronal hole | 20 | 0.67 | 1.4 | $2.7 \times 10^{27}$ |
| XBP | 175 | 2.0 | 1.7 | $3.7 \times 10^{28}$ |



*Figure 9.* Temperature response of image ratios: Fe XII/Fe IX, X (*top*), Fe XV/Fe IX, X (*middle*), and Fe XV/Fe XII (*bottom*).

interpret. Since the emission is a slowly varying function of electron density, a value of $1 \times 10^9$ cm$^3$ is chosen for all the calculations. Values of temperature and emission measure for the polar coronal hole, the base of a plume in the coronal hole and an X-ray bright point are presented in Table IV. Analysis of other structures and other line ratios is not as straightforward.

### 3.1.4. *Temperature Structure of Active Region Loops*
An active region at latitude S 07° and heliographic longitude 260° was observed by EIT from May 1996 to September 1996 (Neupert *et al.*, 1997). By the end of this period it had decayed so that only a neutral line with a quiescent filament bisecting somewhat enhanced magnetic fields of opposite polarity remained. Figure 10 shows the appearance of this region in Fe IX, X and Fe XII as it approached the west limb
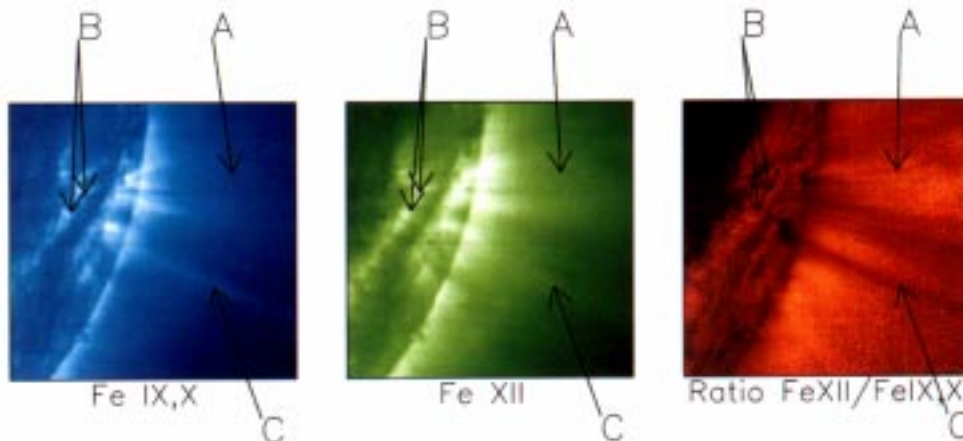
*Figure 10.* Fe IX, X, Fe XII and ratio images for 30 September 1996. Large-scale loops are identified as 'A', small scale loops are identified as 'B' and an extended feature is identified as 'C'.

on 30 September. A complex system of high (200 000 km) loops were present both over the major neutral line, and over leading and trailing portions of the region, where they may have connected to distant weak field regions of mixed polarities. A group of such features, observed most strongly in Fe IX, X and Fe XII, but to a lesser extent in Fe XV (not shown) is indicated as 'A' in the Figure. Smaller loop-like features (several indicated as 'B') were present at lower heights in the central portion of the region. A more nearly radial feature (designated as 'C'), for which only one footpoint was observed, may have been either a very high loop or the base of an open field region extending into the outer corona.

### 3.1.5. *Low Coronal Loops (Height Appreciably Less Than the Separation of Loop Footpoints and the Pressure Scale Height)*

Low loops (less than 10 000–20 000 km) have been observed in their entirety in a one or both spectral bands ('B' in the figure), suggesting that such features are nearly isothermal and in the range of 1.2–1.7 MK. Similar features, although at higher temperatures ($T_e > 2$ MK), have been well-observed by *Skylab*, SMM, and *Yohkoh*.

### 3.1.6. *Large-Scale Loops (Heights to 200 000 km and Comparable to or Greater than Footpoint Separation)*

EIT was able to track several features to heights well in excess of 100 000 km on the limb. The diminution in brightness with height for feature 'A' implies a density scale height of approximately 60 000 km. This result is comparable to the scale height expected at these temperatures. In 'A' the ratio of Fe XII to Fe IX, X increases to a maximum at a height of 190 000 km, suggesting the presence of coronal loops hottest ($T_e = 1.7$ MK) at their tops. Fe XV was also present, although more diffuse, so hotter plasmas may have been intermingled with the loops at 1.2–1.7 MK.

Table V

General characteristics of the 28 December 1996 image sequences
($T$: total duration, $N$: number of images, $\Delta T$: average sampling time)

| Sector | Begin | End | $T$ | $N$ | $\Delta T$ |
|--------|-------|-----|-----|-----|------------|
| He II | $16^h10^m21^s$ | $19^h20^m56^s$ | $3^h10^m35^s$ | 173 | 66.483 s |
| Fe XII | $20^h53^m26^s$ | $21^h59^m08^s$ | $1^h05^m42^s$ | 55 | 70.516 s |

### 3.1.7. *Extended Features*

By comparison with large closed loop feature discussed above, the nearly radial feature denoted by 'C' may have been the base of a magnetically open field region. For this feature the Fe XII/Fe IX, X ratio was less than in the surrounding corona. Diminished emission of Fe XV (not shown) in this feature confirms the relatively low coronal temperature. The pressure scale height in this structure is in the range of 150 000 to 200 000 km. This result is significantly higher than the scale height expected at these temperatures. (N.B. This temperature structure is in contrast to the apparent positive gradient of the plumes in the polar coronal hole.)

### 3.2. INTENSITY OSCILLATIONS IN THE TRANSITION REGION AND CORONA

The EIT's ability to produce high-cadence images covering a wide field of view has brought the picture of a highly dynamical quiet corona, with small-amplitude variations of the local emission at all spatial and time scales. This small-scale activity is observed everywhere and can thus contribute significantly to the energy transfer from the photospheric and chromospheric levels into the corona through the transition region. Movies of the variability of the He II and Fe XII emission are presented in the CD-ROM.

### 3.2.1. *Image Data*

Subimages ($320 \times 320$ pixel) of the central part of the solar disc were sampled every minute on average (unequal sampling) for a total duration of about 3 hours in the He II line and 1 hour in the Fe XII line (Table V). The intensity averaged over the whole data set, with compensation for solar differential rotation, is shown for both sequences in Figure 11. For this first analysis, these corrected images were submitted to a one-dimensional discrete Fourier transform for unequally spaced data (Deeming, 1975) along the time dimension, after an initial preprocessing.

### 3.2.2. *Initial Results*

The dynamics of the solar plasma is expected to vary according to the local state of the plasma, e.g., with magnetic field strength, density and temperature. Changes in these parameters are traced by spatial variations of the EUV brightness, allowing one to distinguish the dark cell interiors and bright cell boundaries in the transition region network, or dim loop patterns and bright points in the corona. In the time-
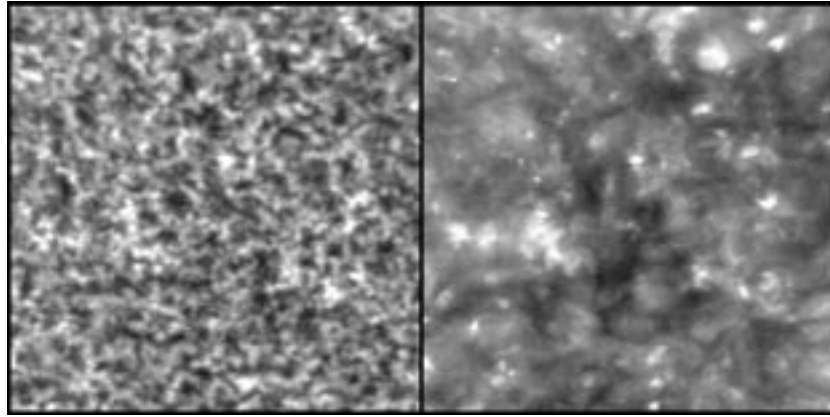
*Figure 11.* Spatial distribution of the average intensity in corrected and projected images of the He II image sequence (*left*) and the Fe XII image sequence (*right*).

averaged intensity maps (Figure 11), the observed contrast and sharpness of small-scale features (network, faint coronal loops) implies a relative stability of the medium-scale magnetic patterns over timescales of the order of the integration time, i.e., several hours.

Taking advantage of this property to improve the signal/noise ratio in the power spectra, individual spectra computed for single pixel locations were grouped by intensity ranges according to the local time-averaged intensity, which reflects the local plasma state. The resulting spectra are dominated by a smooth $f^{-1}$ 'red noise' spectrum. They show only minor changes over the full intensity range, as well in the He II line as in the Fe XII line. The dynamical behavior thus seems largely independent of the local plasma state, and the amplitude of the fluctuations is simply proportional to the local average intensity. This invariance allows us to average out the spectra over the whole field-of-view, further reducing the uncertainty in the power estimates (Figure 12). In these global spectra, the noise background in the 0–2.5 mHz range is accurately reproduced by a $f^{-1.55\pm0.1}$ dependency in He II and $f^{-1.7\pm0.15}$ in Fe XII. These exponent values are close to the $-\frac{5}{3}$ value of the Kolmogorov turbulence spectrum (Landau and Lifchitz, 1971). Such an energy distribution corresponds to a fully developed turbulence (inertial regime) or to an intermittency mechanism in a non-linear system (Schuster, 1984). Spatial variation in the velocities exhibited by the C IV line formed at a temperature similar to the He II were studied by Dere (1989). He found that the power in the velocities varied with the wave number $k$ as $k^{1.5}$ or $k^{5/3}$ as expected for the inertial regime of a turbulent plasma.

For the Fe XII coronal images, the power is falling off more rapidly with frequency, and beyond about 3 mHz the $f^{-1}$ component merges with a uniform white-noise background, indicating the presence of a second noise contribution. Assuming that the fluctuations of the exposure times due to the shutter mechanism
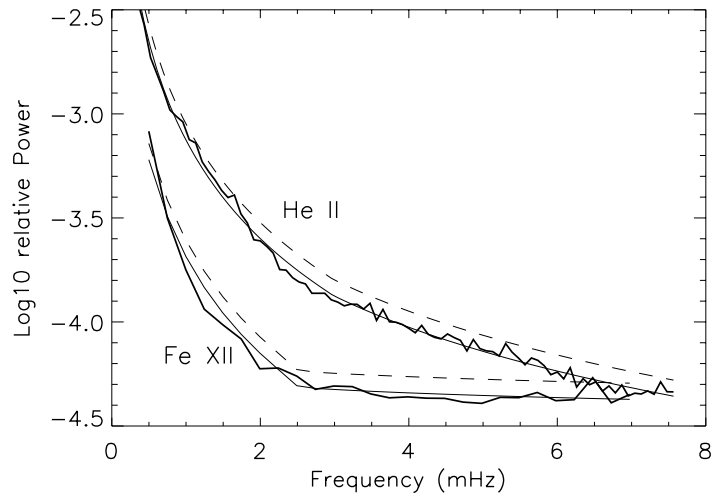
*Figure 12.* Average power spectra computed for the He II (304 È) and Fe XII (195 È) image sequences (full-field average). The thin lines represent the fitted $f^{-1}$ profile, while the dashed lines show the 99.9 confidence levels.

are purely random, the associated 0.4 s standard deviation would correspond to a uniform noise background at a power of $5 \times 10^{-5}$. This is in good agreement with the high frequency part of the Fe XII power spectrum, indicating that this component has an instrumental origin. The same calculation shows that this background is 10 times lower in the He II power spectrum, which is one order of magnitude below the observed background. In this case, the noise background is produced by the Sun over the whole frequency range.

Using chi-squared statistics based on the dispersion of power estimates, the confidence levels (Groth, 1975) were also computed for the power estimates (see Figure 12). No significant local power excess is found, in particular within the 5–min and 3-min period ranges of photospheric and chromospheric oscillations. These oscillations are thus either fully reflected at the base of the corona or strongly attenuated, with residual amplitudes below our detection level. For the present data sets, this level equals 0.4% in relative amplitude. We must also stress that our preliminary study is based on a statistical approach and does not inform us about the spatial coherence of the detected waves. If waves originating in the low atmosphere can only propagate up to the corona along localized vertical magnetic field structures, their signature might elude detection in our spatially averaged spectra. A full 3-dimensional transform as well as the separate analysis of individual features, like single loops or bright points, is thus required and will be applied to the data in a subsequent analysis. Obviously, image sequences produced by EIT will deliver their full content of unique dynamical information only by applying such detailed analysis schemes involving jointly the spatial and temporal dimensions.

3.3. DYNAMICS OF THE POLAR CORONAL HOLE

From previous space observations (e.g., Bohlin, Sheeley, and Tousey, 1975; Ahmad and Webb, 1978; Walker *et al.*, 1993) it was anticipated that EIT observations of structures within the polar coronal hole would contribute to the study of the dynamics of the polar coronal hole. A report by DeForest *et al.* (1997) on coordinated SOHO studies of polar plumes justifies this anticipation and can be found in this volume. The discovery (Gurman *et al.*, 1996) of EUV jetlike events in EIT Fe XII image sequences opens a new perspective on the study of polar coronal hole dynamics. These EUV jet events could be the 'building blocks' of dynamic phenomena in coronal holes.

Figure 13 shows a time series of images taken during the brightest EUV jet event observed so far. This jet begins in a bright, low-lying looplike feature some $1.3 \times 10^4$ km long and extends to the edge of the field of view, over $16.5 \times 10^4$ km above the surface, some 7 min later. During this time, the leading edge of the jet rises at an apparently constant speed of 400 km s$^{-1}$. Measurement of some 15 similar events yields a distribution of average speeds of 100–400 km s$^{-1}$ and maximum observed lengths of 2 to $16.5 \times 10^4$ km. A movie showing an EUV jet eruption is included in the companion CD-ROM.

The EUV jetlike events are similar in appearance to the soft X-ray jets observed with the *Yohkoh* Soft X-ray Telescope (Shibata *et al.*, 1992). While the soft X-ray jets occurred predominantly in active regions and flaring, soft X-ray bright points (Shimojo *et al.*, 1996), the EUV jets appear to be confined to the polar coronal holes. The average speed of the EUV jets in the current (limited) sample, 325 km s$^{-1}$, is higher than that found for 100 soft X-ray jets by Shimojo *et al.* (1996). The maximum observed height of the EUV jets is about half that of the X-ray jets of Shimojo *et al.*'s study. Thus, the EUV jets appear to be a new regime of jet-like phenomena.

The EUV jets are not well observed in the Fe IX, X or the Fe XV channels. The contrast in EIT Fe IX, X images between structures in the coronal hole and the coronal hole itself limits the detection of faint structures. Exposure times in the Fe XV channel for quiet-corona structures are much longer than the other two coronal channels. Fe XV exposures long enough to show the EUV jets would blur these relatively faint features over several pixels, thus raising the brightness threshold for detection.

The footpoints of the microjets constitute a diverse collection of features: low-lying, bright loops as in Figure 13; unresolved structures that vanish as the microjet fades; supergranule-sized areas of emission that eject the microjet helically; and one case (so far) of what appears to be a thin flux tube breaking loose from the solar surface at one end while remaining fixed at the other. All these footpoints appear to have in common is that they occur within a coronal hole, where the magnetic field is diverging, and even small instabilities or eruptions are unlikely to be constrained magnetically.
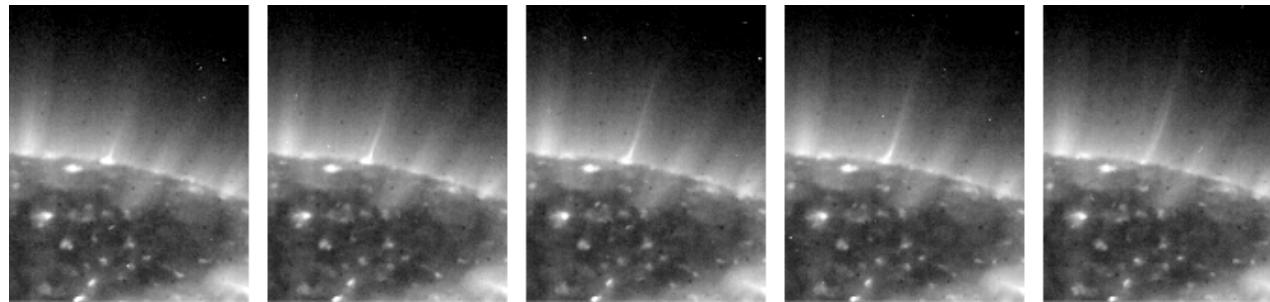
15:48:26          15:50:47          15:53:08          15:55:28          15:57:49

*Figure 13.*  EUV jet in polar coronal hole.

### 3.4. CME watch

With the availability of flexibility in the SOHO telemetry resources beginning in December 1996, it has been possible to initiate sustained high cadence full disk imaging to search for large-scale coronal transients. The instrument is left in a single waveband in order to maximize temporal coverage of phenomena in a single temperature regime. To improve cadence in some circumstance, the resolution is reduced by on-chip binning to improve the cadence while supporting other programs.

During the first CME watch, a CME was observed in Fe XII on 23 December 1996 with full resolution from initiation (Dere *et al.*, 1997). The site of initiation was compact and simultaneously contained a filament eruption, a coronal void, and an outward propagating shock front. This front became the leading edge of the CME observed in LASCO. The evolution of these features is seen in the CME movie on the accompanying CD-ROM.

Associated with this CME was a disturbance tentatively identified as a coronal manifestation of a "Moreton wave". At the time of the initiation of the CME, the event began as a localized increase in emission propagating across the solar disk. The average increase over the entire wavefront began at greater than 10%, decreasing with each successive image. However, individual regions exhibited more than 100% increase in emission.

Based on the five 'coronal Moreton wave' events observed thus far, typical speeds range from 250–400 km s$^{-1}$, and the wavefronts which are initially propagating radially begin to break up and travel in separate fronts. The magnitude of the wave shows little correlation with the peak thermal X-ray flux of the associated event; in fact, the majority of EIT observations close to flare events do not show any evidence of these waves. The model of a weak fast-mode MHD shock developed by Uchida (e.g., Uchida, 1974) explains several features of the EIT observations, including the eventual localization of the wavefronts, the preferential direction of propagation (away from active regions) and the lack of correspondance with the peak thermal X-ray flux of the flare. A movie of a coronal Moreton wave is included in the CD-ROM.

### Acknowledgements

including L. Allen, R. Doney, E. Einfalt, E. Larduinat, J.-P. Olive, S. Passwaters, K. Schenk, H. Schweitzer, S. Stezelberger, and D. Wang. Finally we would like to thank the LASCO team for cooperation in overall operations and the SUMER team for the critical telemetry bandwidth increases they have occasionally allowed EIT.

## References

Ahmad, I. A. and Webb, D. F.: 1978, *Solar Phys.* **58**, 323.

Bohlin, J. D., Sheeley, N. R., and Tousey, R.: 1975, in M. J. Rycroft (ed.), *Space Research*, p. 651.

Bumba, V. and Howard, R.: 1965, *Astrophys. J.* **141**, 1492.

Cheng, C. C., Smith, J. B., and Tandberg-Hanssen, E.: 1980, *Solar Phys.* **45**, 393.

Deeming, T. J.: 1975, *Astrophys. Space Sci.* **36**, 137.

Defise, J.-M. *et al.*: 1997, *SPIE* **3114**, in preparation.

DeForest *et al.*: 1997, *Solar Phys.* **175**, 393 (this issue).

Delaboudinière, J.-P.:1998, *Solar Phys.*, submitted.

Delaboudinière, J.-P., Artzner, G. E., Brunaud, J., Gabriel, A. H., Hochedez, J.-F., Millier, F., Song, X.-Y., Au, B., Dere, K. P., Howard, R. A., Kreplin, R., Michels, D. J., Moses, J. D., Defise, J.-M., Jamar, C., Rochus, P., Chauvineau, J.-P., Marioge, J.-P., Catura, R. C., Lemen, J. R., Shing, L., Stern, R. A., Gurman, J. B., Neupert, W. M., Maucherat, A., Clette, F., Cugnon, P., Van Dessel, E. L. *et al.*: 1995, *Solar Phys.* **162**, 291.

Dere, K. P.: 1989, *Astrophys. J.* **340**, 599.

Dere, K. P. *et al.*: 1997, *Solar Phys.* **175**, 601 (this issue).

Foukal, P.: 1978, *Astrophys. J.* **223**, 1046.

Groth, E. J.: 1975, *Astrophys. J. Suppl.*, No. 286, **29**, 289.

Guhathakurta, M. and Fisher, R.R.: 1994, *Solar Phys.* **152**, 81.

Gurman, J. B. *et al.*: 1996, *EOS* **77**, (46), F557.

Janesick, J. R., Klassen, K. P., and Elliot, T.: 1987, *Opt. Eng.* **26** (10), 972.

Klimchuk, J. A., Moses, D., and Portier-Fozzani, F.: 1997, in preparation.

Klimchuk, J. A., Lemen, J. R., Feldman, U., Tsuneta, S., and Uchida, Y.: 1992, *Publ. Astron. Soc. Japan* **44**, L181.

Kuhn, J. R., Lin, H., and Loranz, D.: 1991, *Publ. Astron. Soc. Pacific* **103**, 1097.

Landau, L. and Lifchitz, E.: 1971, *Mécanique des fluides*, Editions de Moscou.

Moses, D. *et al.*: 1994, *Astrophys. J.* **430**, 913.

Neupert W. M. *et al.*: 1997, *EOS* **78** (17), S256.

Newmark, J.: 1996, *EOS* **77** (46), F557.

Schmahl, E. J. and Orrall, F. Q.: 1979, *Astrophys. J.* **231**, L41.

Schuster, H. G.: 1984, *Deterministic Chaos: An Introduction*, Physik-Verlag, Weinheim.

Schwenn, R. *et al.*: 1997, *Solar Phys.* **175**, 667 (this issue).

Sheeley, N. R.: 1980, *Solar Phys.* **66**, 79.

Shibata, K., Ishido, Y., Acton, L. W., Strong, K.T., Hirayama, T., Uchida, Y.: 1992, *Publ. Astron. Soc. Pacific* **44**, L173.

Shimojo, M., Hashimoto, S., Shibata, K., Hirayama, T., Hudson, H., and Acton, L. W.: 1996, *Publ. Astron. Soc. Pacific* **48**, 123.

Uchida, Y.: 1974, *Solar Phys.* **39**, 431.

Walker, A. B. C., DeForest, C. E., Hoover, R. B., and Barbee, T. D. W.: 1993, *Solar Phys.* **148**, 239.

Webb, D. F.: 1981, in F. Q. Orrall (ed.), *Solar Active Regions*, Colorado Associated University Press, Boulder, p. 165.